Vapor construction and modification of stem cell-laden multicomponent scaffolds for regenerative therapeutics

Yu-Chih Chiang [a,c,e], Hsiao-Wen Yeh [a,f], Shu-Man Hu [b], Chih-Yu Wu [b,c,**], Ting-Ying Wu [b], Chi-Hung Chen [a], Pei-Chun Liao [b], Zhen-Yu Guan [b], Nai-Chen Cheng [d,***], Hsien-Yeh Chen [b,c,*]

[a] School of Dentistry, Graduate Institute of Clinical Dentistry, National Taiwan University and National Taiwan University Hospital, Taipei, 10048, Taiwan
[b] Department of Chemical Engineering, National Taiwan University, Taipei, 10617, Taiwan
[c] Molecular Imaging Center, National Taiwan University, Taipei, 10617, Taiwan
[d] Department of Surgery, National Taiwan University Hospital and College of Medicine, Taipei, 10002, Taiwan
[e] School of Dentistry, Colleage of Dental Medicine, Kaohsiung Medical University, Kaohsiung, 80708, Taiwan
[f] Department of Dentistry, Tri-Service General Hospital, National Defense Medical Center, Taipei, 11490, Taiwan

ABSTRACT

Tissue engineering based on the combined use of isolated cells, scaffolds, and growth factors is widely used; however, the manufacture of cell-preloaded scaffolds faces challenges. Herein, we fabricated a multicomponent scaffold with multiple component accommodations, including bioactive molecules (BMs), such as fibroblast growth factor-2 (FGF-2) and L-ascorbic acid 2-phosphate (A2-P), and living cells of human adipose-derived stem cells (hASCs), within one scaffold construct. We report an innovative fabrication process based on vapor-phased construction using iced templates for vapor sublimation. Simultaneously, the vaporized water molecules were replaced by vapor deposition of poly-*p*-xylylene (PPX, USP Class VI, highly compatible polymer, FDA-approved records), forming a three-dimensional and porous scaffold matrix. More importantly, a multicomponent modification was achieved based on using nonvolatile solutes, including bioactive molecules of FGF-2 and A2-P, and living cells of hASCs, to prepare iced templates for sublimation. Additionally, the fabrication and construction resulted in a multicomponent scaffold product comprising the devised molecules, cells, and vapor-polymerized poly-*p*-xylylene as the scaffold matrix. The clean and dry fabrication process did not require catalysts, initiators or plasticizers, and potentially harmful solvents, and the scaffold products were produced in simple steps within hours of the processing time. Cell viability analysis showed a high survival rate (approximately 86.4%) for the accommodated hASCs in the fabricated scaffold product, and a surprising multilineage differentiation potential of hASCs was highly upregulated because of synergistic guidance by the same accommodated FGF-2 and A2-P components. Proliferation and self-renewal activities were also demonstrated with enhancement of the multicomponent scaffold product. Finally, *in vivo* calvarial defect studies further revealed that the constructed scaffolds provided blood vessels to grow into the bone defect areas with enhancement, and the induced conduction of osteoblast growth also promoted bone healing toward osseointegration. The reported scaffold construction technology represents a prospective tissue engineering scaffold product to enable accommodable and customizable versatility to control the distribution and composition of loading delicate BMs and living hASCs in one scaffold construct and demonstrates unlimited applications in tissue engineering repair and regenerative medicine applications.

1. Introduction

Many surgical procedures are performed to replace or repair tissue that has been damaged because of disease or trauma. Tissue engineering based on combining isolated cells, scaffolds and growth factors is widely used in wound healing, and the regeneration of artificial organs provides

innovative approaches for the repair and regeneration of damaged tissues. Because of the tunable framework, pore size, surface properties, and high surface area, three-dimensional (3D) porous scaffolds render supportive structures and customized environments for cells to mechanically support and guide cell behavior and morphogenesis, requiring few cells while filling defects compared with cells alone. Porous scaffolds provide a large specific surface area for cell adhesion to achieve sufficient cell densities, and additionally, the linked pore structures allow cell movement and distribution across the mass transport and vascularization, which are essential for nutrition exchange and mediating cell behavior [1–5]. A successful scaffold should have appropriate biocompatibility, surface chemistry, porosity and mechanical properties to deliver biomolecules and accelerate the healing process. Therefore, the technique of manufacturing porous scaffolds plays a vital role in tissue engineering. Currently, numerous fabrication methods of porous scaffolds exist, such as gas foaming [6,7], solvent casting and leaching [8], laser sintering [9–12], freeze-drying/lyophilization [13–17], sol-gel, electrospinning [18,19], 3D printing and additive manufacturing [20,21]. However, overcoming the current obstacles to manufacturing cell-loaded scaffolds faces several challenges, including complex protocols and low cell viability, the use of potentially harmful chemicals and solvents, and the injurious effects from removal treatments for many porogens. The use of bioprinting and electrospinning can form a porous scaffold full of layers but cannot simulate the pore complexity of the natural extracellular matrix (ECM) geometry. Furthermore, the need for crosslinking often slows down the bioprinting process and involves chemical modification of ECM materials that can compromise both their chemical and material properties [22]. The technology to date is constrained primarily on a straightforward and simple biochemical function for the constructed scaffold products, and the thriving multifunctional concept to implement a multicomponent scaffold is yet accomplished by a mild and clean fabrication process.

In the present study, we introduced vapor-phased construction of scaffold products, a process that facilitates not only the physical and chemical properties of the scaffolds to better mimic the native ECM but also provides versatility to accommodate sensitive BMs—e.g., growth factors and vitamins, and even living cells—to guide tissue regeneration and cell growth activities. The construction process used simple steps and was based on our previously reported mechanism of vapor sublimation and vapor deposition in the same control volume of a solidified (but volatile—e.g., ice or dry ice) substrate under devised thermodynamic conditions at reduced pressure and temperature to produce a porous and three-dimensional monolith material [23]. The final architecture, interior structure, and mechanical properties, were theoretically tunable and customizable in the range from 5 μm to 100 μm for the pore size, porosity of approximately from 50% to 80%, and a Young's modulus from ~10 kPa to 10000 kPa [24,25]. Therefore, we hypothesized that, through the construction mechanism of vapor sublimation and deposition to define biochemical properties by accommodating BMs, including FGF-2 and A2-P in the scaffold construct, can result in synergistic activities to promote stem cell proliferation activities while maintaining stem cell stemness. Furthermore, mesenchymal stem cells (MSCs) show high potential in cell therapy and regenerative medicine [26]. For example, hASCs are highly abundant in the human body, show high and stable proliferation ability, are of autologous origin to prevent immune rejection, cause minimal discomfort compared with aspiration from the bone marrow, and can be immediately used after isolation [27]. More importantly, the pluripotent nature of hASCs, such as their involvement in adipogenesis, osteogenesis, and hepatogenesis, has been confirmed under both 2D and 3D conditions cultured in specific induction media, and the combination of hASCs and 3D scaffolds is anticipative [28–31]. The same synergistic accommodation hypothesis was finally demonstrated to include living hASCs with selected BMs and enhancing the scaffold properties by the following: (i) high cell viability of the accommodated cells; (ii) a vapor-phased dry and clean process to fabricate the scaffold constructs with highly biocompatible matrix material of poly-*p*-xylylene (United States Pharmacopeia (USP) classified VI polymer, hereafter referred to as PPX); (iii) the versatility to customize components of varying BMs in one scaffold construct to enable defined and guided tissue and cellular activities—e.g., proliferation, self-renewal activities, and varied differentiation pathways; (iv) enhanced osteointegration in an *in vivo* calvarial defect animal model of using the proposed synergistic scaffold constructs fabricated and comprising living hASCs and guiding BMs of FGF-2 and A2-P components. The herein fabricated multicomponent scaffold products with increasing the effectiveness of osseointegration therapeutics are emerging as a prospective bone graft substitute.

2. Materials and methods

2.1. Scaffold fabrication

The bioactive molecules fibroblast growth factor-2 (FGF-2; R&D Systems, USA) and L-ascorbic acid 2-phosphate (A2-P; Sigma-Aldrich, USA) were obtained commercially as indicated. Human adipose-derived stem cells (hASCs) were isolated from subcutaneous adipose tissue according to reported procedures [32], and the protocols were approved by the Research Ethics Committee of National Taiwan University Hospital (REC approval number: 201303038RINB). The cell loading density was 1×10^5 cells per sample, and the culture conditions, including the cell growth medium recipe, were completely based on a previous report [33]. A prepared solution containing FGF-2 (5 μg/mL), A2-P (250 mM) and hASCs (1×10^5 cells) was restricted to a glyceryl trioleate (Sigma-Aldrich, USA) system (oil-in-water system). Next, the solution was loaded into a polydimethylsiloxane (PDMS) mold [34] and cooled with liquid nitrogen during the solidification process. The iced sculptures were taken from the PDMS molds and then placed in a home-built chemical vapor deposition (CVD) system for the proposed scaffold fabrication using the sublimation and deposition process [23, 25]. For the deposition of poly-*p*-xylylene (Parylene™), commercial dichloro-[2,2]-paracyclophane (Galxyl C; Galentis, Italy) was used as received, and the whole enclosed CVD system was vacuumed to approximately 150 mTorr using a vacuum pump. The vapor-phased cyclophane was produced at approximately 100 °C and then pyrolyzed while passing through a pyrolysis zone held at 670 °C by transport with a carrier gas (argon) at a flow rate of 50 sccm, which was controlled by a mass flow controller (MFC; MKS Instruments, USA). The deposition rate was adjusted to approximately 0.4 Å/s, which was monitored using a quartz crystal microbalance (QCM; STM-100/MF; Sycon Instruments, USA).

2.2. Stem cell viability and compatibility

Viability (i.e., the percentage of living cells relative to total cells) of the hASC-accommodated scaffolds was investigated by staining using a LIVE/DEAD kit (Thermo Fisher Scientific, USA). To observe the cell morphology, fabricated samples were dried in an oven overnight, sputtered with a conductive layer of platinum, and recorded using a scanning electron microscopy (SEM) system (Nova™ NanoSEM; FEI, USA) with a primary energy of 10 keV and operating pressure of 5×10^{-6} Torr. To analyze the cell distribution within the fabricated scaffold, the hASCs were first fluorescence labeled with Alexa Fluor® 488-conjugated phalloidin to stain the cytoskeleton and DAPI to stain the nucleus, and the fluorescence images were captured using a confocal laser scanning microscope (TCS SP5; Leica Microsystems, Germany). Furthermore, the 3D fluorescence images were reconstructed using Imaris (version 9.7).

2.3. Material characterization

The microstructural and architectural features of the synthetic porous structures were scanned using a Skyscan 1272 high-resolution micro-CT apparatus (Bruker, Germany) at a pixel size of 2.5 μm and 4-K resolution. The voltage was 40 kVp, and the current was 250 μA at a 10-Watt output. 3D image reconstruction was performed using the reconstruction software GPU-Nrecon (Bruker micro-CT; Kontich, Belgium). The isolated cubes (600*600*600 μm; 267 slices) were then analyzed using CTAn 1.18.4 software (Bruker micro-CT; Kontich Belgium). SEM images were recorded using an SEM system (Nova™ NanoSEM; FEI, USA), and energy-dispersive X-ray spectroscopy (EDS) was further performed to probe the element analysis. The functional groups of the fabricated scaffolds were characterized by infrared reflection absorption spectroscopy (IRRAS) spectra obtained from an FT-IR 100 spectrometer (PerkinElmer, USA) using 128 scans and 4-cm^{-1} resolution with an advanced grazing angle specular reflectance accessory (AGA; PIKE Technologies, USA) and a liquid nitrogen-cooled mercury-cadmium-telluride (MCT) detector.

2.4. Stem cell behavior analysis

The proliferation activity of hASCs was analyzed using a LIVE/DEAD staining kit (Thermo Fisher Scientific, USA) on days 1, 5, and 10 and then was detected using a fluorescence microscope (Leica Microsystems, Germany). The number of viable cells that resided in the scaffolds was further analyzed by the MTT assay (Sigma-Aldrich, USA) following the manufacturer's instructions. Each experiment was performed in triplicate. Using the previously described protocol mainly based on trypsin digestion [35], the cultured hASCs were harvested from the scaffold. For cell surface antigen identification, these hASCs were subjected to interaction with a series of fluorescein isothiocyanate (FITC)-labeled antibodies against human CD34, CD73, CD90 (all from Biolegend, USA), and CD105 (BD-Bioscience, USA) following a previously reported protocol [36] and then were analyzed by flow cytometry (Becton Dickinson, USA). Stemness activity was evaluated on day 7 by immunofluorescence staining and Western blot analysis of the three stem cell pluripotent markers Oct4, Sox2, and Nanog in hASCs following a previously reported protocol [36]. The multilineage differentiation potential of hASCs that housed in the fabricated scaffolds was further verified by incubation in various induction media, as described in previous reports [36,37]. Subsequently, the osteogenic differentiation activity was examined on day 21 based on immunofluorescence staining of the osteogenic marker osteocalcin (OCN). Adipogenic differentiation activity was examined on day 10 by staining with Oil Red O (Sigma-Aldrich, USA) to investigate the lipid droplets. Hepatogenic differentiation capability was analyzed on day 21 according to immunofluorescence staining for the expression of the hepatogenic marker albumin in the differentiated hASCs. Cell nuclei were counterstained with DAPI (4′,6-diamidino-2-phenylindole; Thermo Fisher Scientific, USA). The captured digital images were further analyzed using ImageJ software following the reported method to quantify multilineage activities [38].

2.5. Immunofluorescence and Western blot analyses

Immunofluorescence and Western blot analyses were performed according to a previously described protocol [36] using the following primary antibodies: anti-Oct4 antibody [EPR17980] (Abcam; Cat. No. ab200834; 1:500), anti-SOX2 antibody [9−9−3] (Abcam; Cat. No. ab79351; 1:500), anti-Nanog antibody [EPR2027(2)] (Abcam; Cat. No. ab109250; 1:500), anti-beta actin antibody (Abcam; Cat. No. ab8227; 1:1000), anti-osteocalcin antibody (Abcam; Cat. No. ab198228; 1:200), and anti-human serum albumin antibody (Abcam; Cat. No. ab2406; 1:200) and the following secondary antibodies: goat anti-rabbit IgG H&L (Alexa Fluor® 488) preadsorbed (Abcam; Cat. No. ab150081; 1:200),

goat anti-mouse IgG (whole molecule)−TRITC antibody (Sigma-Aldrich; Cat. No. T5393; 1:200), goat anti-rabbit IgG H&L (HRP) (Abcam; Cat. No. ab6721; 1:2000), and goat anti-mouse IgG H&L (HRP) (Abcam; Cat. No. ab6789; 1:2000).

2.6. Scaffold implantation

The experimental protocol for this animal study was approved by the National Taiwan University College of Medicine and College of Public Health Institutional Animal Care and Use Committee (IACUC20200091). A rat calvarial defect model [39] was used to evaluate the potential of the proposed bioactive scaffolds for regenerative medicine. Seventeen 12-week-old male Wistar rats (BioLASCO Taiwan Co., Ltd, Taipei, Taiwan), with an initial weight of 250–300 g, were used for the animal study. The calvarial cavities of the rats were randomly divided into 3 groups (n = 3): no scaffold (control), scaffold only (PPX), and scaffold with growth factors and hASCs (PPX-hASC-BM). The rats were anesthetized by an intraperitoneal injection of Zoletil (20–40 mg/kg; Virbac, Carros, France) plus xylazine (5–10 mg/kg; Bayer AG, Leverkusen, Germany) before surgery. The calvarium was exposed using a skin incision and periosteum reflection under an aseptic dressing. Two separate full-thickness standardized trephine defects (5 mm in diameter critical-size) were created in the bilateral calvarium under continuous saline buffer irrigation. Extreme care was exercised to avoid damage to the dura mater. The PPX or PPX-hASC-BM graft was implanted into the trephine defect. As a negative control, no graft was inserted after the defects were created. After the defect was treated, the reflected flap was repositioned and sutured. After 8 weeks, the rats were sacrificed with an overdose of pentobarbital, and specimens were harvested and fixed in 10% buffered formalin solution.

2.7. Tissue regeneration

A microcomputed tomography (micro-CT) apparatus (SkyScan 1176; Bruker, Kontich, Belgium) was used to evaluate the calvarial defects. The micro-CT apparatus used an acceleration voltage of 80 kVp and 500 μA with a copper filter. The samples were scanned at a voxel resolution of 36 μm with a rotation of 0.5°. The three-dimensional images were reconstructed, and the region of interest (ROI) was analyzed using the Amira system (Thermo Fisher Scientific, USA). For histological analysis, formalin-fixed samples were trimmed and decalcified in 15% EDTA for 2–3 weeks and then were embedded in paraffin wax. Serial sections of paraffin blocks of 6-μm thickness were obtained along the coronal plane, stained with hematoxylin and eosin (H&E), and then examined under a light microscope (BX51; Olympus Corp., Japan). For immunohistochemistry detection, the sections were incubated with primary antibodies against mouse F4/80 antigen (Thermo Fisher Scientific, USA) and bone sialoprotein (Genetex, USA) at 4 °C overnight. After washing, the sections were coated with a super enhancer at room temperature for 20–30 min using the Super Sensitive™ Polymer-HRP Detection Kit (BioGenex, USA).

2.8. Statistical analysis

All the data were expressed as mean values with standard deviation (mean $\pm$ SD). Significance was set at the 5% level (p < 0.05) using unpaired *t*-test in GraphPad Prism (version 7.0; USA) or ANOVA and LSD post hoc test in IBM SPSS Statistics (version 21.0; USA).

3. Results and discussion

The proposed multicomponent scaffold, as displayed in Fig. 1a, was prepared by the proposed fabrication mechanism via vapor deposition and a sublimation process, as reported previously to construct porous
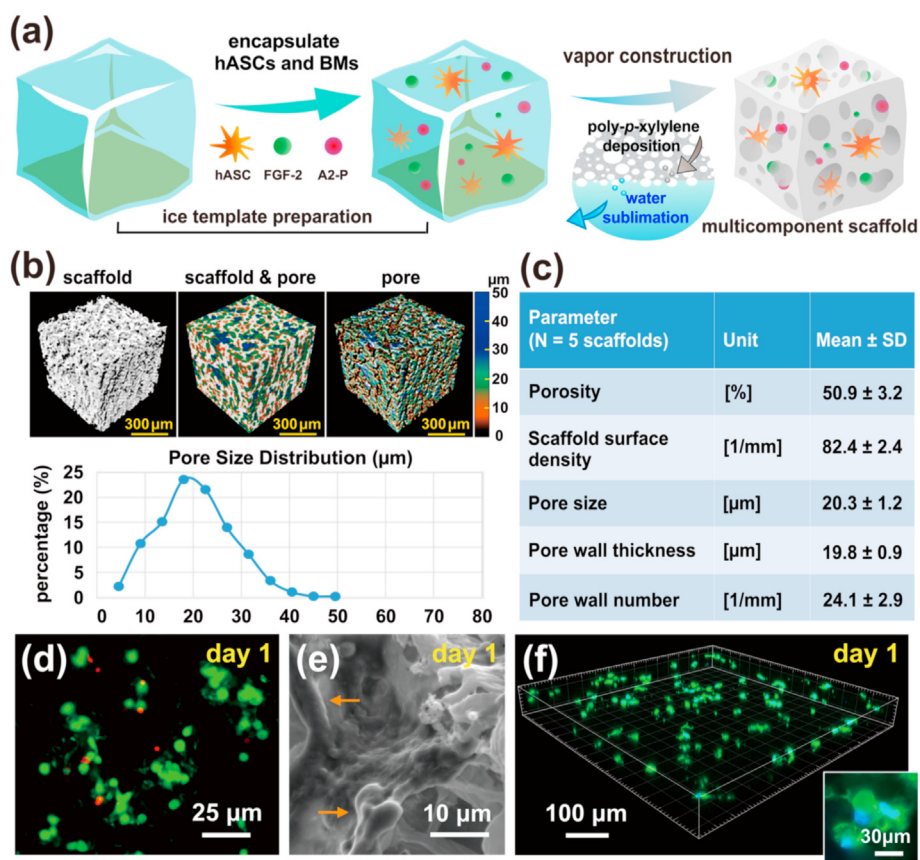
Fig. 1. Scaffold fabrication and characterization. (a) Proposed manufacturing process using controlled mass transport during vapor-phased sublimation/ deposition to construct a multicomponent scaffold and simultaneously accommodated human adipose-derived stem cells (hASCs) and multiple bioactive molecules of fibroblast growth factor-2 (FGF-2) and L-ascorbic acid 2-phosphate (A2-P). (b) Micro-CT imaging of the manufactured scaffold showed a porous structure and interconnected pores. The measured pore size distribution ranged from 5 to 50 μm. (c) Scaffold morphometrical properties (N = 5 scaffolds) assessed by micro-CT analysis. (d) The cell viability assessed by LIVE/DEAD staining analysis at day 1 showed that approximately 86.4% of the accommodated hASCs were alive and emitted green fluorescence in the fabricated scaffold. Dead cells were stained in red for comparison. (e) The SEM image of the interior structure showed that the accommodated hASCs adhered and grew on the manufactured porous scaffold. (f) The 3D confocal micrograph further showed that the accommodated hASCs were evenly distributed in the fabricated scaffold. hASCs were fluorescence labeled with Alexa Fluor® 488-conjugated phalloidin to stain the cytoskeleton (green) and DAPI to stain the nucleus (blue); a high resolution and magnified image of stained cells is shown in the inset.

PPX particles [23,40] and three-dimensional bulk materials [25]. Briefly, an iced substrate was prepared by solidifying a water solution, which served as a sublimating template under controlled thermodynamic conditions at approximately 0 °C and 100 mTorr. Simultaneously, vapor-phase deposition of PPX occurred on the same sublimating template (under the same conditions), and the bidirectional mass transfers showed water molecule sublimation out of the system and quinodimethane (precursor of PPX) deposition into the system. The process resulted in the transformation of the water component into a PPX porous matrix in the same volume space. Unlike the traditional chemical vapor deposition process of PPX on a nonsublimating and stationary surface, which should result in a dense thin film coating of PPX [41–43], the deposition on this sublimating surface resulted in a three-dimensional and porous monolith structure of PPX. Theoretically, unlimited dopant components can be introduced to ice templates and are encapsulated in porous PPX during the described vapor deposition and sublimation process [23,40]. Thus, in the experiment, multiple doping components to prepare iced templates included the following: (i) BMs of fibroblast growth factor-2 (FGF-2) and L-ascorbic acid 2-phosphate (A2-P), which promoted stem cell proliferation activities and the self-renewal of multiple differentiation potentials through PI3K/AKT and MEK/ERK signaling and hepatocyte growth factor expression [44]; (ii) living hASCs that exhibit excellent genetic characteristics of pluripotency and avoid ethical concerns of high potential for stem cell therapy [26]. A low vapor pressure oil, glyceryl trioleate, was used specifically to form (ii) an oil-in-water system to protect hASCs during the reduced temperature and pressure conditions of the process. The resulting suspension of water solution that comprised (i) and (ii) was then subjected to a solidification procedure using a liquid nitrogen bath and converted into the described ice template. Subsequently, in the deposition system where the thermodynamic conditions were controlled at 0 °C and 100 mTorr, the introduction of vapor-phased quinodimethane precursors into the system produced favorable deposition of PPX on the cooled substrate of the sublimating ice template. Using the aforementioned vapor sublimation and deposition mechanism, a porous scaffold containing encapsulated (i) and (ii) components and PPX as the matrix was constructed. A real-time mass spectrometric gas analyzer was used to monitor the vapor composition during the vapor sublimation and deposition process. Figure S1 (Supporting Information) reveals a characteristic peak at 18 amu representing the sublimated water molecule from the ice template, and peaks at 104 amu and 138 amu indicated *p*-quinodimethanes and derivatives, showing evidence of PPX deposition.

Characterization of the resulting scaffold was further performed by microcomputed tomography (micro-CT; Fig. 1b). The three-dimensional images recorded by micro-CT showed a relatively uniform porous scaffold product, and the interconnected pores were approximately $99.94 \pm 0.01\%$. The measured pore size distribution ranged from 5 to 50 μm, most of which were approximately 20 μm (accounting for 24% of all pores). Because of the sublimation of water vapor and three-dimensional fractal and nucleated polymerization, the proposed manufacturing method can form interconnected porous structures [25]. Most importantly, the nature of the interconnected pores is considered crucial to the transport and exchange gradients for signal factors, gases, nutrients, and bioactive molecules to achieve the best prospects for the proliferation and tissue-like assembly of cultured cells [45]. Fig. 1c further summarizes the morphometrical characteristics of the fabricated scaffold by micro-CT analysis (N = 5 scaffolds). The scaffolds showed a medium porosity of $50.9 \pm 3.2\%$ to provide adequate mechanical support. The average scaffold surface density (SS/TV) that plays a role in cell attachment and growth was 82.4 ± 2.4 mm^2 mm^{-3}. The resulting pore size (20.3 ± 1.2

μm on average) and pore wall thickness (19.8 ± 0.9 μm) provided the scaffold with the proper strength and environment for cell proliferation and differentiation. Additionally, the pore wall number averaged 24.1 ± 2.9 mm^{-1} in this interconnected porous scaffold. Despite the aforementioned versatility of adjusting mechanical properties, which were also reported elsewhere [24,25], and in order to constrain the focus on the conceptual integration of multicomponent biochemical properties of the scaffold fabrication technique, mechanical parameters of the fabricated scaffold products were maintained with consistency, including approximately a 42.3 ± 7.3 μm in pore size, 71.2% ± 5.8 for the porosity, and a 221 ± 19.3 kPa Young's modulus, were characterized and utilized in the experiments.

From a material chemistry perspective, Fourier transform infrared spectroscopy (FT-IR) analysis, as indicated in Figure S2 (Supporting Information), and the recorded spectra showed characteristic absorption peaks for PPX: C¬H peaks at 2924 cm^{-1}, 2863 cm^{-1}, 1407 cm^{-1} to 1590 cm^{-1} for the aromatic $C{=}C$ stretching peaks and collective peaks at approximately 878 cm^{-1} for the C¬Cl bands. Furthermore, the peak of enol-hydroxyl ($C{=}O{\neg}OH$) and stretching vibration $C{=}C$ double bond at 1322 cm^{-1} and 1391 cm^{-1}, respectively, were attributed to A2-P. More importantly, confirmation peaks revealing the accommodated FGF-2 and A2-P were also successfully detected, showing $N{\neg}H$ and O¬H peaks collectively from 3200 cm^{-1} to 3600 cm^{-1}, and strong peaks at approximately 1655 cm^{-1} for the characteristic $C{=}O$ asymmetric stretching bands were also discovered for the two accommodated

molecules, which were consistent compared with the literature results [46,47]. Observation and cell viability analysis of the accommodated hASCs by LIVE/DEAD staining at day 1 in Fig. 1d shows that approximately 86.4% were alive based on the ratio of total viable cells to total cells. The results were comparable to the previous report with the cell viability based on the proposed vapor sublimation and deposition fabrication process showed approximately 98.2% (in oil-in-water suspension), 96.1% (after freezing in ice templates), and 80.8% (after fabrication in the final scaffold constructs) [48]. This result not only confirmed the physiological state of the accommodated cells but also supported that the proposed nondestructive manufacturing process can accommodate living cells and obtain a highly compatible cell-loaded scaffold construct. The qualitative and quantitative analyses of the 3D micro-CT dataset combined with the SEM images, as shown in Fig. 1e, taken at day 1 provided more insight into the multicomponent scaffold and confirmed that the pore size was in the range of 15–30 μm. The SEM image also provided important evidence that the manufactured PPX matrix of the porous scaffold is compatible with the attachment and growth of hASCs. Additionally, the accommodated hASCs were fluorescently labeled with Alexa Fluor® 488-coupled phalloidin to stain the F-actin cytoskeleton (green) and DAPI to stain the nucleus (blue) and showed a uniform distribution in the manufactured scaffold, as displayed in the 3D confocal image in Fig. 1f. The image also showed that the proposed manufacturing process enables the accommodated hASCs to achieve more coordinated functions through cell-cell and cell-matrix
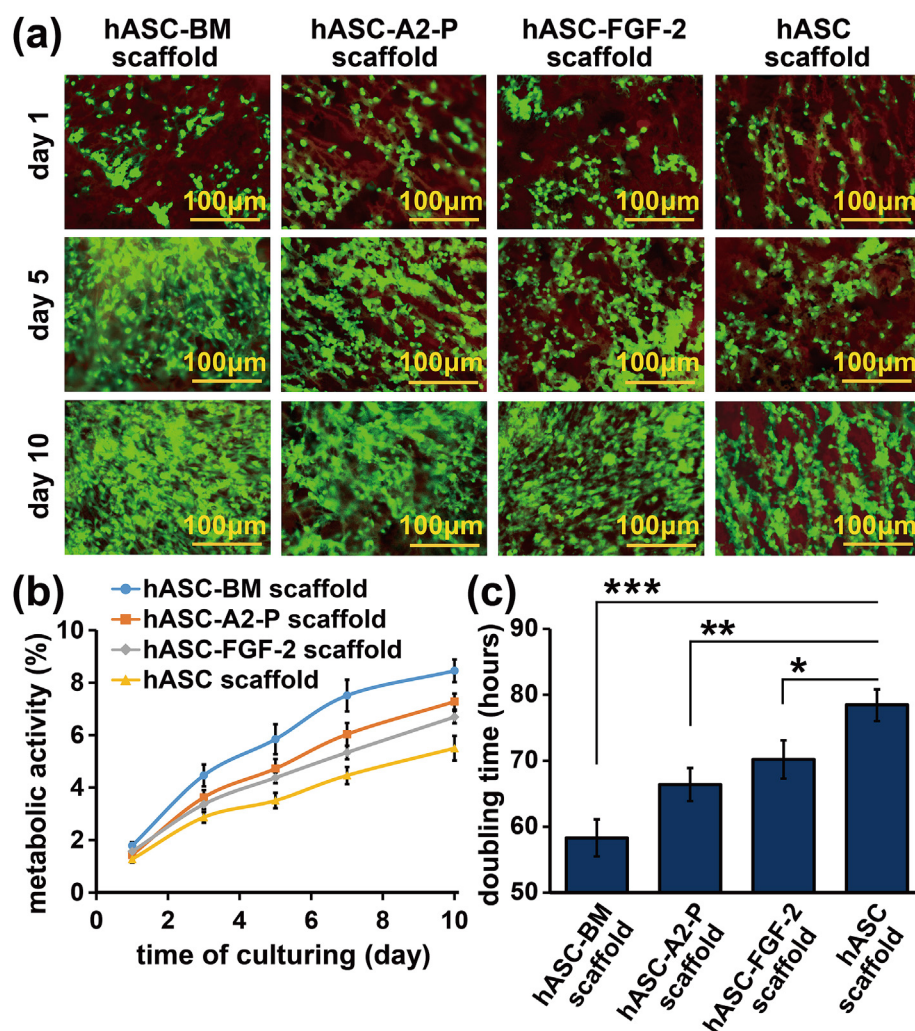

Fig. 2. Cell proliferation behavior analysis. (a) Cell morphology and growth pattern on the fabricated scaffolds that accommodate specific bioactive molecules (BMs) and living hASCs. The viable and proliferating hASCs (green channel) were visualized by LIVE/DEAD staining at days 1, 5, and 10. The red background was mainly the reflection of the noise signal on the surface of the scaffold. Compared with other studied scaffolds, the scaffold containing FGF-2 and A2-P (i.e., hASC-BM scaffold) had the best effect on enhancing cell proliferation. (b) The metabolic activity curves of the accommodated hASCs were determined using the MTT assay. (c) The doubling time required for the logarithmic growth of the accommodated cell population was further calculated and compared. The statistical data are expressed as mean values ± standard deviation based on three independent samples (*: p-value < 0.05; **: p-value < 0.01; ***: p-value < 0.001, compared to the hASC scaffold group).

interactions, which in turn help promote cell integrity, viability, and proliferation [49,50].

With negligible cytotoxicity during the fabrication process and the high compatibility demonstrated on the fabricated scaffold products, the proposed multicomponent PPX scaffold was further confirmed to have a functionalized microenvironment that promotes stem cell proliferation, self-renewal and differentiation. By analyzing the cells by LIVE/DEAD staining at days 1, 5, and 10, the cell growth patterns on the scaffolds modified/decorated with hASCs and specific bioactive molecules were characterized, as shown in Fig. 2a. Compared with day 1, live cells (green channel) and more proliferating cells of the cultured hASCs were found on day 5 and day 10. Notably, a synergistic effect appeared when the scaffold accommodated both FGF-2 and A2-P (i.e., hASC-BM scaffolds), enhancing cell proliferation. The red background was the reflection of a noise signal on the surface of the scaffold; by contrast, the dead cells were stained with much brighter red signals and appeared as a few small red spots. As shown in Fig. 2b, the metabolic activity cell growth curves were determined by the MTT assay, and the statistical results confirmed that, although either FGF-2 or A2-P can promote cell population growth, these two molecules work better together, indicating a synergistic effect. Additionally, the doubling time required for the logarithmic growth of the cell population of the scaffold samples with or without accommodation of the bioactive molecules was compared, as displayed in Fig. 2c. The doubling time for hASC growth on the scaffold decorated with FGF-2 and A2-P was the shortest, further supporting the above suggestion of synergistic enhancement. Phenotypic identification of isolated hASCs was performed using flow cytometry to determine the expression profile of cell surface antigens [37]. As shown in Figure S3 (Supporting

Information), the surface epitopes of hASCs isolated from the scaffold decorated with FGF-2 and A2-P (i.e., hASC-BM scaffolds) were similar to those of the hASCs isolated from the control group (i.e., hASC scaffolds). These cells were showed positivity for the mesenchymal stem cell related markers (CD73, CD90, and CD105) and negativity for the hematopoietic/immune cell marker (CD34). The results clearly confirmed that the housed hASCs predominantly showed mesodermal or mesenchymal characteristics without obvious blood and endothelial cell contamination.

To further confirm the hypothesis that the self-renewal/stemness property was upregulated by the modified FGF-2 and A2-P for the accommodated hASCs in the fabricated multicomponent scaffolds, the cultured hASCs were harvested from the scaffolds by trypsinization on the 7th day and then the immunofluorescence and Western blot analyses were used to examine the expression of the pluripotent marker proteins Oct4, Sox2 and Nanog. As shown in Fig. 3a, the low expression levels of all three proteins detected in the control group (i.e., hASC scaffolds) that do not accommodate FGF-2 and A2-P indicate that hASCs on such scaffolds quickly lose their original stemness properties during *in vitro* propagation. By contrast, the stronger expression of the pluripotent marker protein of hASCs was confirmed in the proposed manufactured scaffold that accommodates FGF-2 and A2-P (i.e., hASC-BM scaffolds). More importantly, as shown in Fig. 3b and c, Western blot analysis of Oct4, Sox2, and Nanog proteins proved that the stemness of hASCs in FGF-2 and A2-P decorated samples was enhanced, and the protein band intensity quantified using ImageJ software further confirmed the significantly enhanced expression, with higher levels of Oct4 (1.20-fold more), Sox2 (1.17-fold more), and Nanog (1.28-fold more) than those of the
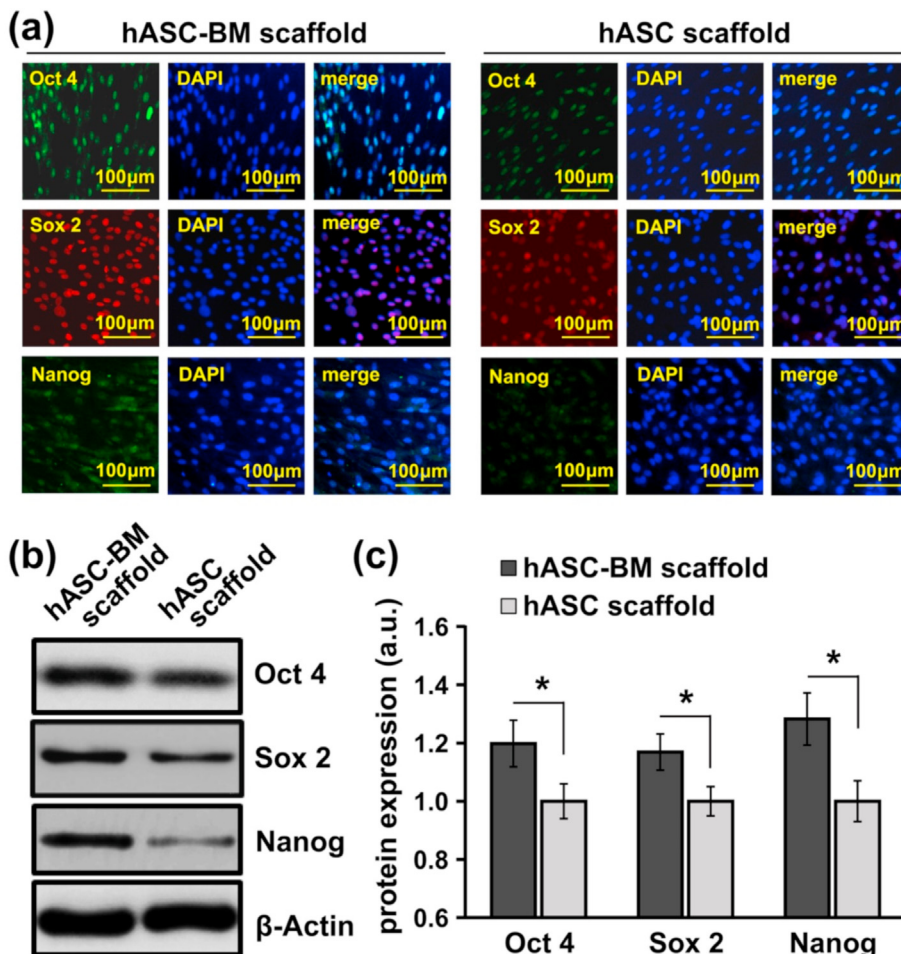
Fig. 3. Cell self-renewal marker expression. (a) Immunofluorescence of stem cell pluripotent markers Oct-4, Sox-2 and Nanog showing the stem cell guidance property on the fabricated scaffolds that accommodate specific bioactive molecules (BMs) and living hASCs. After 7 days of culture, the fabricated scaffold containing A2-P and FGF-2 molecules (i.e., hASC-BM scaffold) enhanced the self-renewal activities of accommodated hASCs. These hASCs were harvested from the scaffolds by trypsinization and analyzed with approximately the same number of cells. All the nuclei were counterstained with DAPI (blue channel) to guide imaging. For comparison, a control scaffold (i.e., hASC scaffold) containing hASCs within the pure PPX matrix was used in parallel. (b) Western blot analysis of Oct4, Sox2, and Nanog proteins. β-Actin served as an internal protein loading control. (c) Quantification of the band intensity using the densitometric analysis software ImageJ. The data are presented as the mean relative density ± SD of three independent experiments; *: p-value < 0.05, compared to the hASC scaffold group.
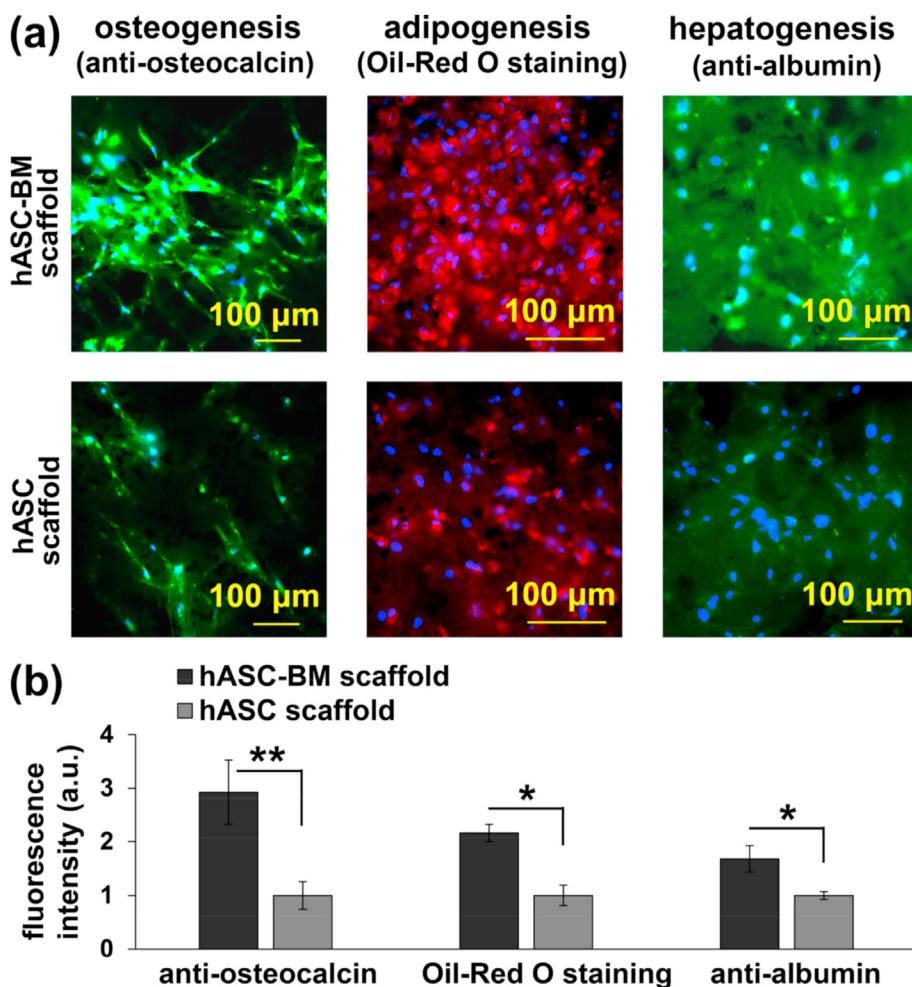
Fig. 4. Cell differentiation potential analysis. (a) The multilineage differentiation capabilities of hASCs, including osteogenesis, adipogenesis, and hepatogenesis, were confirmed by anti-osteocalcin immunofluorescence staining at day 21, Oil Red O staining at day 10, and anti-albumin immunofluorescence staining at day 21, respectively, on the fabricated scaffold accommodated with A2-P and FGF-2 molecules (i.e., hASC-BM scaffold) compared with a control scaffold (i.e., hASC scaffold) containing hASCs within the pure PPX matrix. The nucleus (blue) was counterstained with DAPI to indicate the cell position. (b) Quantification of fluorescence intensity using the image analysis software ImageJ. The data are presented as the mean relative fluorescence density $\pm$ SD of three independent experiments; *: p-value < 0.05 and **: p-value < 0.01, compared with the control group.

control samples. These results confirmed the hypothesis that the proposed multicomponent PPX scaffold decorated with FGF-2 and A2-P had a synergistic effect to promote the self-renewal/stemness of the housed stem cells.

Furthermore, the proposed multicomponent PPX scaffold decorated with FGF-2 and A2-P was confirmed to provide a synergistic niche to enhance pluripotency (i.e., multilineage differentiation ability) of the contained stem cells. As displayed in Fig. 4a, osteogenic activity was examined by anti-osteocalcin immunofluorescence staining after 21 days of culture in osteogenic medium. The fabricated scaffold group modified with FGF-2 and A2-P (i.e., hASC-BM scaffolds) exhibited a stronger fluorescent signal for osteocalcin expression than the control group (i.e., hASC scaffolds), which does not accommodate FGF-2 and A2-P. In comparison to previous reports, characterizations by examining the alkaline phosphatase (ALP) activities were also shown with upregulated enhancement based on using similar poly-p-xylylene platform with BMP-2 or PRP (platelet-rich plasma) modifications [51–54], and are unambiguously comparable to the results in the current work. Adipogenic activity was examined by Oil Red O staining after 10 days of culture in adipogenic medium. Compared with the control group (i.e., hASC scaffolds), more oil droplets (shown as red particles) were found in the fabricated scaffold decorated with FGF-2 and A2-P (i.e., hASC-BM scaffolds). Hepatogenic activity was further examined by anti-albumin immunofluorescence staining after 21 days of culture in hepatogenic medium, and the scaffolds decorated with FGF-2 and A2-P (i.e., hASC-BM

scaffolds) had stronger fluorescent signals for albumin expression than the control group (i.e., hASC scaffolds). Similarly, on the fabricated scaffolds decorated with FGF-2 and A2-P, the typical polygonal cells were larger and expressed more albumin, indicating a higher level of hepatic differentiation [55,56]; on the control scaffolds without FGF-2 and A2-P, a relatively small cell volume and low albumin expression were observed, indicating that the level of hepatic differentiation was suppressed [55, 56]. Furthermore, quantification of fluorescence intensity was performed using the image analysis software ImageJ (Fig. 4b). The fabricated scaffolds decorated with FGF-2 and A2-P exhibited significantly enhanced multilineage differentiation activities, with higher levels of osteogenesis by anti-osteocalcin immunofluorescence staining (2.92-fold more), adipogenesis by Oil red O staining (2.16-fold more), and hepatogenesis by anti-albumin immunofluorescence staining (1.68-fold more) compared to the control group, which does not accommodate FGF-2 and A2-P. These results not only proved a synergistic effect of FGF-2 and A2-P to enhance the multilineage differentiation ability of stem cells but also unambiguously confirmed that the proposed manufacturing process could construct a multicomponent scaffold decorated with defined bioactive molecules to guide the differentiation of accommodated stem cells. Furthermore, the promising potential of diversified lineages indicates that the manufactured multicomponent scaffold containing living hASCs and bioactive molecules may be a promising medical product for the regenerative treatment of diseases and tissue abnormalities.
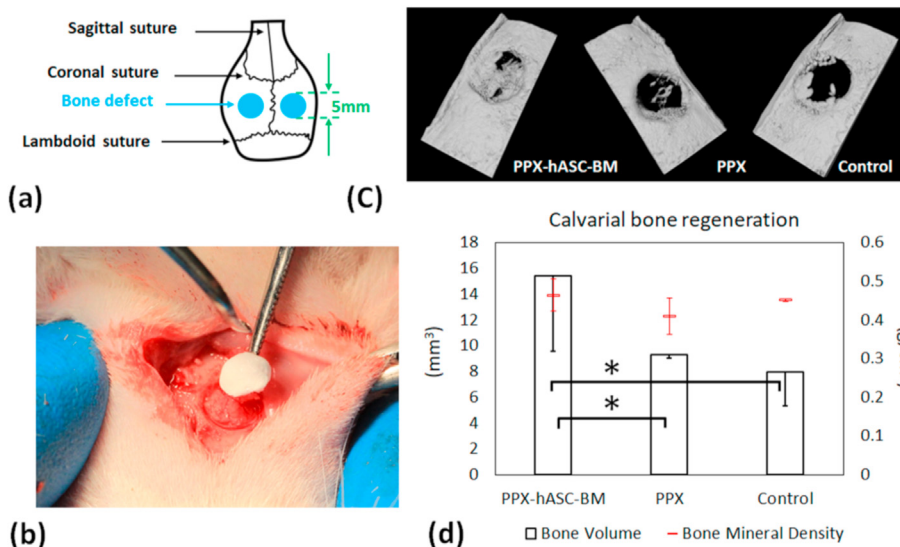
Fig. 5. Overview and micro-CT imaging evaluation of calvarial bone defects of animal study (rat). (a) Outline of the experimental design of rat calvarium. Bone trephine defects (5 mm in diameter critical-size) were made at the bilateral calvarium. (b) Calvarial bone defects were created, and the scaffold was implanted. (c) New bone formation evaluation of 3D micro-CT image reconstruction at 8 weeks post-operatively. PPX: poly-*p*-xylylene-based porous scaffold, PPX-hASC-BM: FGF-2/A2-P-treated and hASC accommodated PPX, Control: no scaffold used in trephine defects. (d) Bone volume and mineral density calculated from micro-CT 3D datasets using Amira software, asterisk (*) indicated statistically significant difference ($p < 0.05$). No significant difference was found in bone mineral density.

To prove the potential in tissue engineering repair and regenerative medicine applications *in vivo*, the fabricated multicomponent scaffold accommodating living hASCs and bioactive molecules, including FGF-2 and A2-P, was used as a bone graft in a rat calvarial defect model. Fig. 5a and b shows 5-mm critical-size trephine defects on the bilateral calvaria and the graft placed in the bone cavity. The 3D micro-CT datasets were segmented and further analyzed using Amira software (Thermo Fisher Scientific, USA) for quantitative and qualitative evaluations. The PPX-hASC-BM scaffolds in trephine defects grew approximately 45 vol% more mineralized tissue than those of the control group ($p < 0.05$). From micro-CT imaging analysis, we found a clear difference between using a scaffold and not in the critical-size trephine defect. Without a scaffold in the calvarial bone cavity, the bone tissue always started growing from the border and bottom of the defect area, and the central area was always filled with hemorrhage and fibrous tissue and presented radiolucent images on micro-CT (Figs. 5c and 6a). Additionally, connective tissue scar formation retarded the bone healing process, particularly in critical-size bone defects (Fig. 6a). However, the presence of PPX and its derived scaffold (i.e., PPX-hASC-BM scaffolds) promoted the blood vessels to grow into the scaffold (Fig. 6b; HE stains) and allowed multiple bone tissue deposits in the center area of the calvarial bone cavity (Fig. 5c). The scaffold accommodated with hASCs will even accelerate the maturation of bone tissue. The underlying mechanism of tissue regeneration used in this study is different from the traditional concept, that is, the accommodated hASCs are cells that directly form new tissues. Instead, the accommodated hASCs can be regarded as "medicinal cell factories", indicating that they secrete many bioactive molecules, including proteins, nucleic acids, proteasomes, exosomes, microRNA and membrane vesicles, collectively referred to as the secretome. They then respond to the surrounding microenvironment to recruit osteogenic and endothelial progenitors, promote cell proliferation, osteoblast differentiation, and angiogenesis, and inhibit inflammation and apoptosis [57,58]. Several small animal model studies have shown that even the use of a heterologous secretome from hASCs or hMSCs can promote bone regeneration [59–61]. More importantly, these results clearly demonstrate the potential of the proposed multicomponent scaffold for stem cell therapy-based regenerative medicine.

The histology analysis supported the findings of micro-CT and HE staining showed using PPX-hASC-BM scaffolds resulted in multiple new bone matrix depositions in the middle of the calvarial trephine defect and formed numerous bone trabeculae along with bone marrow (Fig. 6c). At 4 weeks with PPX implanted in calvarial bone defects (Fig. 6b), abundant blood vessels were found in new bones and bone marrow, indicating that the PPX scaffold can provide a highly biocompatible channel for cells and form a source of nutrients for osteogenesis. Using FGF-2/A2-P and hASCs, osteogenesis in the critical-size defect and its osteogenesis efficacy were even more apparent, as expressed by the BSP marker (Fig. 6c; BSP staining). The abundance of preosteoblasts, osteoprogenitor cells, and collagen in the bone marrow also implied that osteogenesis occurred during a period of highly active bone metabolism and modeling. To detect F4/80, the control model (no scaffold) showed little macrophage infiltration, while neither macrophage nor inflammatory cell were found in the PPX scaffold and PPX-hASC-BM scaffold (Fig. 6c; F4/80 detection). Thus, our surgical procedure was aseptically controlled, and the PPX scaffold or PPX-derived bioactive scaffolds also displayed a highly biocompatible scaffold *in vivo*. The histological analysis results proved that the multicomponent scaffold can promote blood vessel growth in bone and create an environment for bone building and regeneration, regulating immunity and inflammation. These findings further confirmed that the accommodated hASCs can be regarded as "medicinal cell factories" to exert the above-mentioned therapeutic effects with the aid of FGF-2 and A2-P molecules. Collectively, the multicomponent scaffold represents a promising scaffold construction technology that provides the potential to realize adaptability and customizable versatility of loading delicate BMs and living hASCs with defined composition. Additionally, in a single scaffold construct, the proposed fabrication mechanism and multicomponent scaffold products are expected with unlimited applications in tissue engineering repair and regenerative medicine.

4. Conclusions

Scaffolds with increasing sophistication in multiple functions and stringent specifications were investigated to fabricate modern tissue engineering products. The encountered challenges indicate complicated problems to deal with multiple molecules during fabrication and cell culture *in vitro* and *in vivo*. The reported scaffold construct demonstrated a facile engineering approach to accommodate multiple functional molecules and living cells during a single vapor-phase fabrication process
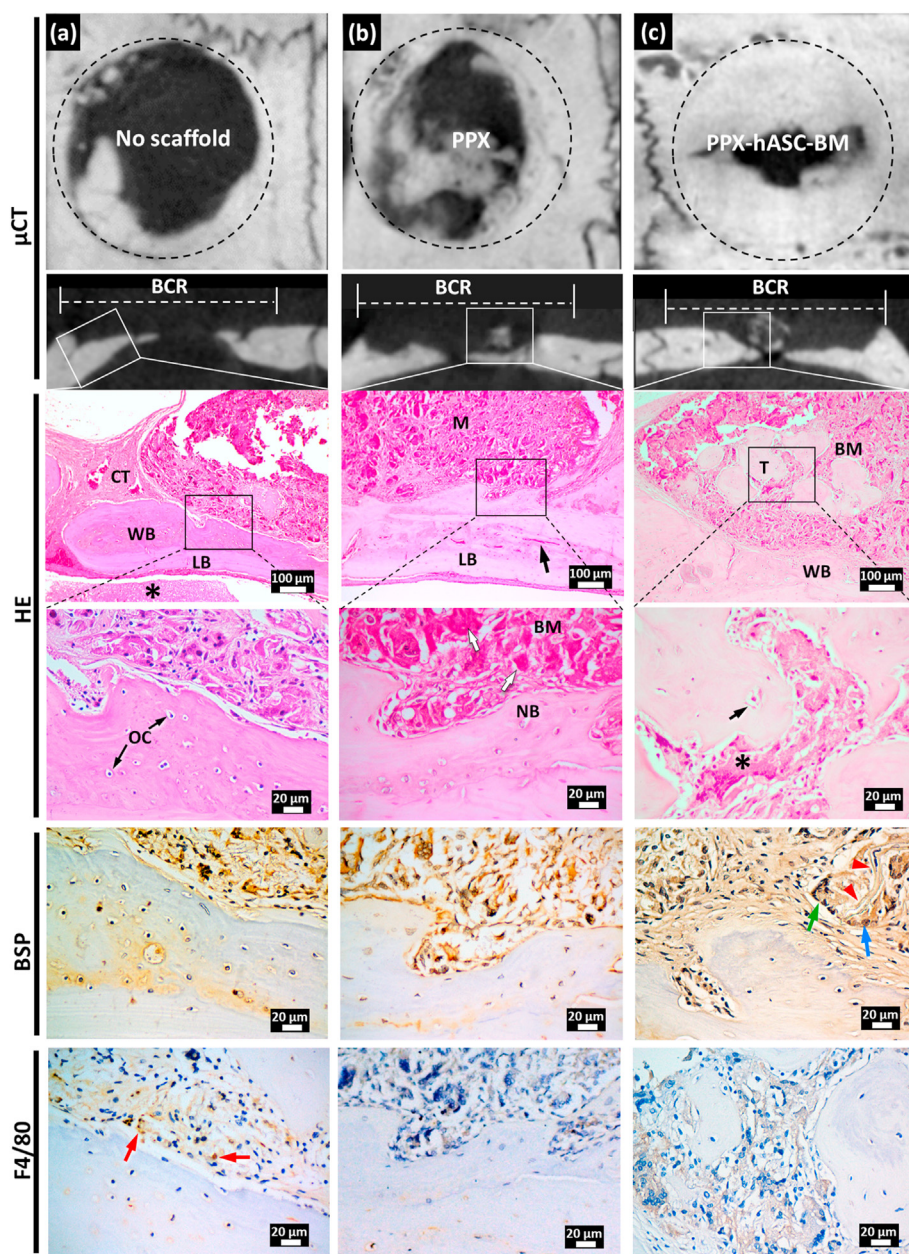
Fig. 6. Representative micro-CT images and histology analyses of calvarial bone regeneration at trephine defects. (HE: hematoxylin and eosin stain; BSP: bone sialoprotein stain; F4/80: F4/80 antibody stain for macrophage markers). (a) No scaffold was used in the bone window at 8 weeks postsurgery. Micro-CT image showed the bone formed along the peripheral margin of the bone cavity wall. Mature laminar bone (LB) formed at the bottom of the bony cavity. Osteocytes (OCs) were clearly shown in woven bone. Fibrous connective tissue (CT) with hemorrhage was found at the margin of the bone cavity. Brain tissue (*asterisk) at the bottom of the picture. BSP staining showed osteoblasts making bone in the bone marrow and along the woven bone. Few macrophages were detected (red arrows). (b) Nonfunctionalized pure PPX scaffold used in a bone window at 8 weeks postsurgery. The micro-CT image showed that new mineralized bone deposition occurred in the middle and peripheral areas of the trephine defect. Lamellar bone (LB) formed on the borders. Newly mineralized bone matrix (M) and bone marrow (BM) filled in the center. Red blood cells in capillaries (black arrow) formed in BM. Groups of osteoclasts were noted (white arrows). Promyelocytes and myelocytes were found in the bone marrow. Osteoclasts and osteoblasts surrounded a new bone matrix (NB). No inflammatory cell infiltration was observed (F4/80 detection) at this stage. (c) Proposed living cell- and bioactive molecule-loaded scaffolds (PPX-hASC-BM) used in the bone window at 8 weeks postsurgery. Micro-CT images showed new bone tissue formed in the middle of the trephine defect. More mature bone formed along the peripheral area of the bone cavity. A Haversian canal (black arrow) was formed in trabecular bone. Furthermore, numerous osteoprogenitor cells and collagen (*asterisk) were observed between new bones in which osteocytes were lining. An intense reaction was observed between trabecular bones stained for BSP. A fragment of the PPX scaffold (red arrowheads) was surrounded by preosteoblasts (blue arrow) and osteoprogenitor cells (green arrow). No macrophage or lymphocyte/plasma cell infiltration was found (F4/80 detection).

without complicating the molecular interactions, representing an engineering approach to achieve a highly compatible matrix and biochemical microenvironment for enhanced stem cell viability and thus upregulated multiple activities. We foresee the reported scaffold fabrication technology is extendable beyond the demonstrated FGF-2/A2-P/hASC system and is expected to facilitate a more sophisticated scaffolding system with advantages of optimizing cell number, cell types, functional biomolecules, and mechanical properties, for prospective tissue engineering and regenerative therapy applications.

Credit author statement

Yu-Chih Chiang, Nai-Chen Cheng, Hsien-Yeh Chen: **Conceptualization.** Yu-Chih Chiang, Chih-Yu Wu: **Methodology.** Hsiao-Wen Yeh, Shu-Man Hu, Ting-Ying Wu, Chi-Hung Chen, Pei-Chun Liao, Zhen-Yu Guan: **Data curation.** Yu-Chih Chiang, Nai-Chen Cheng, Chih-Yu Wu, Hsien-Yeh Chen: **Writing- Original draft.** Hsiao-Wen Yeh, Shu-Man Hu, Ting-Ying Wu, Chi-Hung Chen, Pei-Chun Liao, Zhen-Yu Guan:

Visualization, **Investigation.** Yu-Chih Chiang, Nai-Chen Cheng, Hsien-Yeh Chen: **Supervision.** Hsiao-Wen Yeh, Shu-Man Hu, Chih-Yu Wu, Ting-Ying Wu: **Validation.** Yu-Chih Chiang, Nai-Chen Cheng, Hsien-Yeh Chen, Shu-Man Hu, Chih-Yu Wu: **Writing- Reviewing and Editing**.

Supporting Information

Vapor composition and XPS analysis, FT-IR characterizations, flow cytometric analysis of surface antigen expression.

Data availability

All data generated or analyzed during this study are included in this published article and its supplementary information files.

Declaration of competing interest

The authors declare that they have no known competing financial

interests or personal relationships that could have appeared to influence the work reported in this paper.

Acknowledgments

Appendix A. Supplementary data

Supplementary data to this article can be found online at https://doi.org/10.1016/j.mtbio.2022.100213.

References

[1] K. Arvidson, et al., J. Cell Mol. Med. 15 (4) (2011) 718.
[2] Y. Yamada, et al., Tissue Eng. 10 (5–6) (2004) 955.
[3] M. Whitaker, et al., J. Pharm. Pharmacol. 53 (11) (2001) 1427.
[4] Z. Wang, et al., NPG Asia Mater. 9 (10) (2017) e435.
[5] T.M. De Witte, et al., Regen Biomater 5 (4) (2018) 197.
[6] T.K. Kim, et al., Biomaterials 27 (2) (2006) 152.
[7] Z.W. Ma, et al., J. Biomed. Mater. Res. B Appl. Biomater. 67B (1) (2003) 610.
[8] C.J. Liao, et al., J. Biomed. Mater. Res. 59 (4) (2002) 676.
[9] J.M. Williams, et al., Biomaterials 26 (23) (2005) 4817.
[10] K.H. Tan, et al., Biomaterials 24 (18) (2003) 3115.
[11] S. Eshraghi, S. Das, Acta Biomater. 6 (7) (2010) 2467.
[12] R.D. Goodridge, et al., Prog. Mater. Sci. 57 (2) (2012) 229.
[13] S. Deville, R.K. Nalla, Science 312 (5778) (2006) 1312.
[14] L. Ma, et al., Biomaterials 24 (26) (2003) 4833.
[15] H.W. Kang, et al., Biomaterials 20 (14) (1999) 1339.
[16] M.H. Ho, et al., Biomaterials 25 (1) (2004) 129.
[17] X.H. Zhao, et al., Proc. Natl. Acad. Sci. U. S. A 108 (1) (2011) 67.
[18] S.R. Jang, et al., Materials Science & Engineering C-Materials for Biological Applications 111 (2020) 13.
[19] W.J. Li, et al., Acta Biomater. 2 (4) (2006) 377.
[20] S.J. Hollister, Nat. Mater. 4 (7) (2005) 518.
[21] F. Pati, et al., Nat. Commun. 5 (2014) 11.
[22] S.V. Murphy, A. Atala, Nat. Biotechnol. 32 (8) (2014) 773.
[23] H.-Y. Tung, et al., Nat. Commun. 9 (1) (2018) 2564.
[24] Y.-R. Chiu, et al., Chem. Mater. 32 (3) (2020) 1120.
[25] H.-Y. Tung, et al., Applied Materials Today 7 (2017) 77.
[26] Y. Han, et al., Cells 8 (8) (2019).
[27] J.M. Gimble, et al., Circ. Res. 100 (9) (2007) 1249.
[28] L. De Girolamo, et al., Int. J. Artif. Organs 31 (6) (2008) 467.
[29] J. Guo, et al., Mol. Med. Rep. 16 (4) (2017) 4095.
[30] E. Canciani, et al., J. Craniofac. Surg. 27 (3) (2016) 727.
[31] R. Nieto-Aguilar, et al., J. Biomater. Appl. 25 (7) (2011) 743.
[32] B.A. Bunnell, et al., Methods 45 (2) (2008) 115.
[33] S.T. Chen, et al., ACS Appl. Mater. Interfaces 10 (38) (2018) 31882.
[34] H.-Y. Chen, J. Lahann, Adv. Mater. 19 (22) (2007) 3801.
[35] W. Jia, et al., Int. J. Oncol. 52 (6) (2018) 1787.
[36] C.-Y. Wu, et al., Adv. Mater. Interfac. 4 (11) (2017).
[37] J.S. Yu, et al., Biomaterials 35 (11) (2014) 3516.
[38] C.A. Schneider, et al., Nat. Methods 9 (7) (2012) 671.
[39] J.A. McGovern, et al., Dis Model Mech 11 (4) (2018).
[40] Y. Shi, et al., ACS Biomater. Sci. Eng. 6 (4) (2020) 1836.
[41] P. Simon, et al., Macromolecules 31 (25) (1998) 8775.
[42] J.B. Fortin, T.M. Lu, Chem. Mater. 14 (5) (2002) 1945.
[43] H.-Y. Chen, J. Lahann, Langmuir 27 (1) (2010) 34.
[44] S.H. Bae, et al., Growth Factors 33 (2) (2015) 71.
[45] S. Pina, et al., Materials 12 (11) (2019).
[46] C. Yohannan Panicker, et al., Spectrochim. Acta Mol. Biomol. Spectrosc. 65 (3) (2006) 802.
[47] S.J. Prestrelski, et al., Arch. Biochem. Biophys. 285 (1) (1991) 111.
[48] C.-Y. Wu, et al., Nat. Commun. 12 (1) (2021) 3413.
[49] I.C. Ng, et al., Anatomy and physiology for biomaterials research and development, in: R. Narayan (Ed.), Encyclopedia of Biomedical Engineering, Elsevier, Oxford, 2019, p. 225.
[50] Q. Wei, H. Huang, Chapter five - insights into the role of cell–cell junctions in physiology and disease, in: K.W. Jeon (Ed.), International Review of Cell and Molecular Biology, vol. 306, Academic Press, 2013, p. 187.
[51] C.-Y. Wu, et al., Coatings (5) (2021) 11.
[52] C.-Y. Wu, et al., ACS Applied Bio Materials 3 (10) (2020) 7193.
[53] Y.-T. Tsai, et al., Biomaterials Science 4 (12) (2016) 1754.
[54] Z.-Y. Guan, et al., ACS Appl. Mater. Interfaces 8 (22) (2016) 13812.
[55] M. Wang, et al., Tissue Eng. C Methods 16 (5) (2010) 1041.
[56] M.J. Seo, et al., Biochem. Biophys. Res. Commun. 328 (1) (2005) 258.
[57] H.R. Hofer, R.S. Tuan, Stem Cell Res. Ther. 7 (1) (2016) 131.
[58] A.I. Caplan, Stem Cells Transl Med 6 (6) (2017) 1445.
[59] M. Osugi, et al., Tissue Eng. 18 (13–14) (2012) 1479.
[60] W. Li, et al., ACS Appl. Mater. Interfaces 10 (6) (2018) 5240.
[61] Y. Zhang, et al., Cell Prolif 52 (2) (2019), e12570.